PCCP

Softening by charging: how collective modes of ionic association in concentrated redoxmer/electrolyte solutions define the structural and dynamic properties in different states of charge

Journal:	*Physical Chemistry Chemical Physics*
Manuscript ID	CP-ART-09-2022-004220.R1
Article Type:	Paper
Date Submitted by the Author:	19-Dec-2022

Complete List of Authors:	Farag, Hossam; University of Illinois Urbana-Champaign, Nuclear, Plasma, and Radiological Engineering Kaur, Aman; University of Kentucky, Chemistry Robertson, Lily ; Argonne National Laboratory, Chemical Sciences and Engineering Division; University of Illinois at Urbana-Champaign, School of Chemical Sciences Sarnello, Erik; Northern Illinois University, Department of Chemistry and Biochemistry Liu, Xinyi; Northern Illinois University, Chemistry and Biochemistry Wang, Yilin; University of Illinois at Urbana-Champaign, Mechanical science and engineering Cheng, Lei; Argonne National Laboratory, Materials Science Division Shkrob, Ilya; Argonne National Laboratory, Chemical Sciences and Engineering Zhang, Lu; Argonne National Laboratory, Chemical Science & Engineering Ewoldt, Randy; University of Illinois at Urbana-Champaign, Li, Tao; Northern Illinois University, Department of Chemistry and Biochemistry Odom, Susan; University of Kentucky, Chemistry Yang, Z. H.; University of Illinois at Urbana-Champaign, Nuclear, Plasma, and Radiological Engineering, Department of Materials Science and Engineering, Department of Electrical and Computer Engineering

ARTICLE

Softening by charging: how collective modes of ionic association in concentrated redoxmer/electrolyte solutions define the structural and dynamic properties in different states of charge

Received 00th January 20xx,
Accepted 00th January 20xx

DOI: 10.1039/x0xx00000x

Hossam M. Farag,[a,b,c] Aman Preet Kaur,[a,d] Lily A. Robertson,[a,e] Erik Sarnello,[a,g] Xinyi Liu,[a,g] Yilin Wang,[a,c,h] Lei Cheng,[a,f] Ilya A. Shkrob,[a,e] Lu Zhang,[a,e] Randy Ewoldt,[a,c,h] Tao Li,[a,i,g] Susan A. Odom,[a,d] Y Z*,[a,b,c,j]

ABSTRACT: Understanding the physical and chemical processes occurring in concentrated electrolyte solutions is required to achieve redox flow batteries with high energy density. Highly concentrated electrolyte solutions are often studied, in which collective crowded interactions between molecules and ions become pre-dominant. Herein, experimental, and computational methods were used to examine non-aqueous electrolyte solutions in two different states of charge as a function of redoxmer concentration. As the latter increases and the ionic association strengthens, the electric conductivity passes through a maximum and the solution increasingly gels, which is seen through a rapid non-linear increase in viscosity. We establish that the structural rigidity of ionic networks is closely connected with this loss of fluidity and show that charging generally yields softer ionic assemblies with weaker attractive forces and improved dynamical properties.

Introduction

In electrochemical flow cells, redox active molecules (redoxmers) are used as charge carriers in a liquid electrolyte, so the energy density of the fluid is proportional to the redoxmer concentration. This consideration underlies the current interest to concentrated electrolyte solutions of the redoxmers. During electrochemical cycling, the redox active molecules are present in different states of charge, to store electric energy. The electrolyte provides the medium for charge transport between the electrodes required to sustain redox reactions on the electrodes.[1] In the hydrodynamics framework, in which only collective motion is considered, the transport of mass, momentum, and electric charge is defined by the respective transport coefficients, namely diffusivity, fluidity, and ionic conductivity. For obvious reasons, these coefficients need to remain high during charge and discharge to facilitate operation of the cell. While these solutions have macroscopic homogeneity, we are interested in their physico-chemical properties as functions of temperature and concentration.[2–6] Linking the results with molecular-scale structure and interactions is imperative to mastering design of these complex functional solutions.[7]

The dynamics of ions in electrolyte solutions has been studied theoretically by many pioneers including Lars Onsager who introduced the principle of microscopic reversibility and contributed towards understanding the ionic atmosphere.[4–6,8,9] The problem has also received many reviews due to its practical importance.[3,10–15] However, the analytical approaches largely fail to accurately describe the properties of concentrated electrolytes, while the computational approaches overly depend on a delicate balance between the interactions in each specific system.[3] As the main culprit is collective interactions occurring in these systems, better understanding of these interactions is direly needed.[3]

Several studies using classical molecular dynamics (MD) simulations in conjunction with experimental techniques have advanced our understanding of concentrated non-aqueous electrolytes.[16–20] A generalized framework based on ion solvation has been proposed to rationalize the observed bulk dynamical properties of electrolytes.[21,22] To give examples,

[a] Joint Center for Energy Storage Research
[b] Department of Nuclear, Plasma, and Radiological Engineering, University of Illinois at Urbana–Champaign, Urbana, Illinois 61801, United States
[c] Beckman Institute for Advanced Science and Technology, University of Illinois at Urbana–Champaign, Urbana, Illinois 61801, United States
[d] Department of Chemistry, University of Kentucky, Lexington, Kentucky 40506, United States
[e] Chemical Sciences and Engineering Division, Argonne National Laboratory, Lemont, Illinois 60439, United States
[f] Materials Sciences Division, Argonne National Laboratory, Lemont, Illinois 60439, United States
[g] Department of Chemistry and Biochemistry, Northern Illinois University, DeKalb, Illinois 60115, Unites States
[h] Department of Mechanical Science and Engineering, University of Illinois at Urbana–Champaign, Urbana, Illinois 61801, United States
[i] X-ray Science Division, Argonne National Laboratory, Lemont, Illinois 60439, United States
[j] Department of Electrical and Computer Engineering, University of Illinois at Urbana–Champaign, Urbana, Illinois 61801, United States
Electronic Supplementary Information (ESI) available: [details of any supplementary information available should be included here]. See DOI: 10.1039/x0xx00000x

Henderson and co-workers have examined the transport properties of nonaqueous electrolytes,[23–26] while Dang and co-workers have examined the effect of varying the anion and the organic solvent on the solvation and ion pair kinetics of lithium cations.[16,20] High ionic concentration in the electrolytes results in local electric fields polarizing solvent and ions that often require either explicit or mean-field inclusion of polarization effects, especially for sampling non-equilibrium structures.[27] Despite rapid advances in modeling of the binary electrolytes, the solvation and association in ternary electrolytes containing redox active molecules in different states of charge lags behind.[28–32] Here, we seek to close this gap.

In this study, computational and experimental approaches are used to examine the solution structure and dynamics of the electrolyte systems chosen for their practical relevance, as representatives of the 0% and 100% states of charge (SOC) in one compartment of a redox flow battery.[11,33,34]

The neutral (fully discharged) solution in this compartment consists of an equimolar mixture of *N*-(2-methoxyethoxyethyl) phenothiazine (MEEPT) and lithium bis(trifluoromethyl)sulfonimide (LiTFSI) electrolyte in acetonitrile (MeCN). In a flow cell, MEEPT is a catholyte that stores positive charge. The simulated charged solution consists of MEEPT radical cations (charged MEEPT molecules) paired with $TFSI^-$ anions. This is equivalent to assuming that during electrochemical charging, lithium cations migrate from the MEEPT compartment across a selective Li^+ conducting membrane separating the two compartments. This ideal ion exchange membrane blocks all other species including the solvent molecules. While these assumptions are not realistic, they allow us to simulate cell fluids without making the additional assumptions regarding cell design and experimental conditions. We emphasize that no electrochemically charged solutions were used in our experimental studies: the simulated charged solutions were composed using chemically oxidized MEEPT ($MEEPT^{+\bullet}TFSI^-$ salt). In the following, we will simply call these simulated cell fluids neutral (0% SOC) and charged (100% SOC) solutions as they contain neutral and charged MEEPT molecules, respectively. The reason we chose parity between the MEEPT and LiTFSI molarities in the neutral solution is that charging of MEEPT requires pairing of $MEEPT^{+\bullet}$ with $TFSI^-$ anions, which in our idealized cell originate from the same cell compartment; i.e., for full charge the concentration of the salt needs to be greater or equal the concentration of the redoxmer. If the salt is in molar excess, at high concentration there is stronger association between the electrolyte ions resulting in lower viscosity and conductivity, so this excess needs to be minimized.

The viscometric properties of MEEPT in different electrolytes have been reported by Ewoldt and co-workers.[35] Here, we extend this study to examine the effect of redoxmer charging on ionic conductivity, viscosity, and diffusivity, in addition to providing insight into the interactions responsible for the observed behaviors.

Materials and Methods

Refinement of Born-Oppenheimer Potential Energy Surface

Density functional theory (DFT) calculations were performed using the NWChem[36] suite to refine the Born–Oppenheimer potential energy surface of the novel synthesized redox-active molecules, in terms of their equilibrium molecular conformation and partial charges on each ionic center. The geometries and electrostatic potentials for acetonitrile, bistriflimide anion, and phenothiazine MEEPT/$MEEPT^{+*}$ molecule/radical cation were optimized using DFT with the B3LYP[37,38] hybrid functional with 6-31/G(d,p) Gaussian type orbital basis set. The implicit solvent density based SMD model[39] was used to represent the solvent in these DFT calculations. A grid-based fitted electrostatic potential energy surface was used to estimate the partial atomic charges on each ion.

The partial atomic charges were proportionally scaled to best agree with experimentally measured ionic conductivity σ (see below). This renormalization was shown to be suitable to mimic the electronic charge fluctuations caused by the polarization of solvent molecules surrounding the charged and/or polar solutes, which in turn renders the charged and/or polar solutes more polar and screens the Coulomb field of the surrounded solute from other solution charged and/or polar species.[40] Another electronic effect we mimic using charge renormalization in our electronically coarse-grained simulations is the charge transfer reactions between the solvent and solutes. Figure 1 shows the structural representations of $TFSI^-$ anion and MEEPT molecules in their neutral and radical cation states, and the potential iso-surfaces.

Molecular Dynamics Simulations

Classical MD simulation was used to probe the solution structure and dynamics. All simulations were carried out using Gromacs 2019.5.[41] The van der Waals parameters and intramolecular interactions were based on the OPLS-AA [42]

force field. Geometric average combining rules were used for interatomic mixings of both of Lennard-Jones (L-J) parameters. Superimposed is the electrostatic interaction with the prescribed partial atomic charges. Based on the obtained refined electronically coarse-grained model, MD simulations with a time step between 1 and 2 fs were performed. First, simulation boxes were prepared with a fixed edge length of ~10 nm. We packed a range of 8250 to 1700 molecules of MeCN with 50 to 1088 solute molecules corresponding to solute molarity *c* = 0.11 to 2.11 M. Second, the solvent molecules and dissociated solutes were randomly placed in a periodic cubic box using Packmol.[43] The steepest descent energy minimization was performed to remove unrealistic contacts occurring in this random configuration. Subsequent simulations in the NPT ensemble for 5 ns with 1 fs time-step were carried out to obtain the average equilibrium density of the solution mixture. The pre-equilibration molarities were slightly varied with volume relaxation in NPT simulations. Then, the obtained equilibrium volume was used to re-run the simulation in the NVT ensemble for 4 ns equilibration, then for 50 ns production run to obtain statistical averages.

We have chosen the cutoff distances r_{cut} = 1.2 nm for all simulations. The leap-frog integrator was used in all runs. For simulations in the NPT ensembles, a modified-Berendsen thermostat[44] and a Parrinello-Rahman barostat[45] were used to equilibrate the system at 1 bar and 298 K. For simulations in canonical NVT ensembles, a modified-Berendsen thermostat was used. [44] Particle-mesh Ewald summation[46] was used for all long-range Coulomb interactions.

Statistical Analyses

Statistical errors were calculated from block averaging, and errors of the calculated values were obtained from error propagations of the individual block averaging errors. All computations were performed using the LiquidLib suite developed by the UIUC group.[47]

To characterize the solution molecular structure, we computed the center-of-mass radial pair distribution function (PDF),

$$\boldsymbol{g(r) = \frac{1}{4\pi r^2 dr \rho N}\left\langle \sum_{l \neq l'}^{N} \delta(r - |r_l - r_{l'}|) \right\rangle}$$

(1)

where $\boldsymbol{\rho}$ is the system-average species density, $\boldsymbol{N}$ is the total number of species, $\boldsymbol{r}$ is the radial distance from the tagged particle center-of-mass, and $\langle \cdots \rangle$ denotes the ensemble average.

We also derived the potential, $\boldsymbol{W(r)}$, of the solution-averaged mean force (PMF) from the PDF, $\boldsymbol{g(r)}$, defined as

$$\boldsymbol{W(r) = -k_B T \ln\left(g(r)\right)}$$

(2)

where $\boldsymbol{k_B}$ is Boltzmann constant and $\boldsymbol{T}$ is the temperature. The Green-Kubo relations were used for the computation of transport coefficients, namely

$$\boldsymbol{\sigma = \frac{1}{3Vk_BT}\int_0^\infty \langle J\,(t=0)\cdot J\,(t)\rangle dt}$$

(3)

$$\boldsymbol{\eta = \frac{V}{k_BT}\int_0^\infty \langle \Sigma_{xy}\,(t=0)\,\Sigma_{xy}\,(t)\rangle dt}$$

(4)

where $\boldsymbol{\sigma}$ is the ionic conductivity, $\boldsymbol{\eta}$ is the dynamic viscosity, $\boldsymbol{V}$ is the system volume, $\boldsymbol{J}$ is the electrical current, $\boldsymbol{\Sigma_{xy}}$ is the system off-diagonal elements of the stress tensor. We also computed the infinite-frequency dynamic modulus $\boldsymbol{G_\infty}$ defined as,

$$\boldsymbol{G_\infty = \frac{V}{k_BT}\langle \Sigma_{xy}\,(t=0)\,\Sigma_{xy}\,(t=0)\rangle}$$

(5)

where all symbols are defined as above.

Experimental Details

Materials

The synthesized phenothiazine redoxmers used in this study were prepared according to methods found in previous literature.[48–55]

Conductometry and Diffusivity Measurements

The ionic conductivity $\boldsymbol{\sigma}$ of electrolyte solutions was determined using a miniature conductivity probe with blocking platinum electrodes. A sequence of bipolar pulses was used to estimate ohmic resistance, and standard salt solutions were used to calibrate the cell and convert this resistance to conductivity. To measure molecular and ionic

diffusivity, pulsed field gradient nuclear magnetic resonance (NMR) was used. For MeCN and MEEP, proton NMR was used, while for Li^+, and $TFSI^-$, lithium-7 and fluorine-19 resonance was used, respectively. The details of these methods are given in ref. [56]. Due to paramagnetism of $MEEPT^{+\bullet}$, NMR measurements were only possible in neutral MEEPT solutions.

Viscometry

The dynamic viscosity $\boldsymbol{\eta}$ was measured using a microchannel viscometer (Rheosense), in which the liquid sample flows through a rectangular channel with a controlled flow rate and the pressure drop is measured using micromechanical sensors. The details were mentioned in refs.[57–60] All solutions studied are Newtonian within the shear rate < $3x10^4$ s^{-1}, due to small size of solutes and short viscoelastic relaxation times.[60]

Small-angle X-ray scattering (SAXS)

SAXS experiments were acquired at the Advanced Photon Source (APS) 12ID-B and C station of Argonne National Laboratory (ANL). The data were collected on a Pilatus 2 M area detector (DECTRIS) and an incident photon energy of 13.3 keV. 1.5 mm diameter quartz capillary tubes containing liquid samples were sealed with epoxy glue in a glove box. More details are given in refs.[61,62]

Results and Discussions

Figures 1a and 1b show the schematic representation of the two systems in different states of charge. Figure 1a shows the neutral solution, which is composed of 1:1 mol/mol MEEPT:LiTFSI in MeCN. In the simulated charged solution, each molecule of MEEPT becomes a radical cation in the $MEEPT^{+\bullet}TFSI^-$ salt, while the Li^+ cations migrate across the separator membrane to maintain overall charge neutrality (Figure 1b). The Li^+ migration increases the molarity of charged MEEPT due to the volume previously occupied by the solvated Li^+ ions, so one would compare different molarities in different states of charge to capture the effect of charging on the solution properties. Since Li^+ is a small ion, this correction is relatively small, about 5% at > 2 M, which is in the supersaturated metastable region. For practical purposes, we have made the comparisons on similar molarities for the two solutions, and we included the molarity corrections in the SI Figure 1 for quantitative comparisons in the supersaturated regime. All drawn conclusions and discussion are not qualitatively affected by such approximation. In the plots below, blue and red are consistently used for the neutral and charged solutions, respectively.

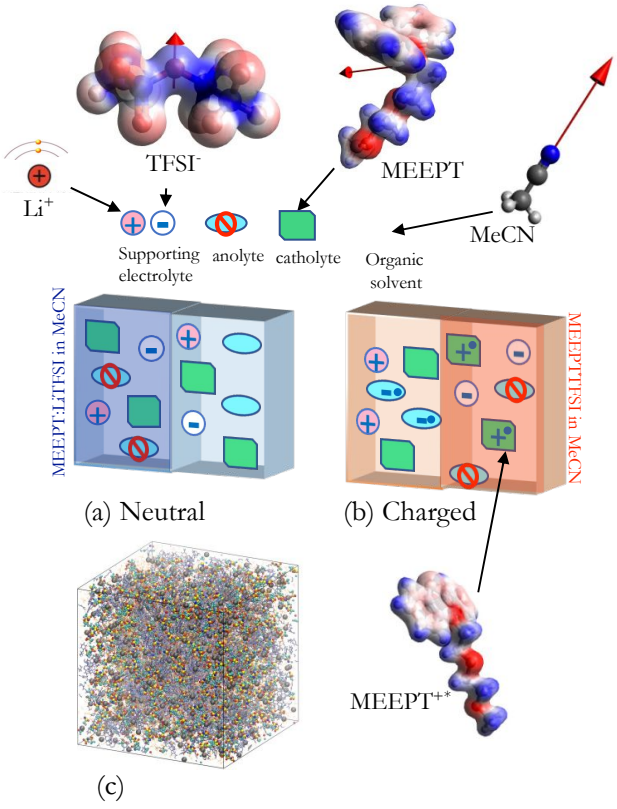

Figure 1. Non-aqueous electrolyte in a cell compartment shown in different states of charge. Anolytes, which are the negatively charged redoxmers, are omitted from the current study. (a) MEEPT and Li^+TFSI^- in MeCN representing the cell at full discharge. (b) $MEEPT^{+\bullet}TFSI^-$ representing the cell at full charge. (c) A screen shot of the MD simulation box.

Ionic conductivity and dynamic viscosity

Figure 2 shows the ionic conductivity and dynamic viscosity plotted as a function of molarity *c* of the redoxmer. As seen in Figure 2a, the ionic conductivity first increases with *c* due to the increasing concentration of charge carriers. It reaches a maximum value at c_{crit}~0.7 M and then decreases. The maximum approximately coincides with the onset of non-linear increase in dynamic viscosity shown in Figure 2b. The molecular mechanism of this increase, which accelerates as the solution thickens further, is what we aim to elaborate in this study. For $c > c_{crit}$, the ionic conductivity of charged solution is higher compared to the neutral solution of the same molarity. This implies that the cell performance (e.g., internal resistance) changes considerably with the state of charge. Notably, this difference becomes less pronounced at lower concentrations, and it becomes negligible in dilute solutions. According to ref [63] and SI Figure 2 in such solutions the Li^+ ion is chelated by two oxygens in the polyether chain of MEEPT (this chelation persists across the entire

concentration range). Thus, one can consider the neutral solution as a mixture of $TFSI^-$ anions and MEEPT:Li^+ cation complexes, explaining the similarity in the molar ionic conductivity in the dilute solutions.

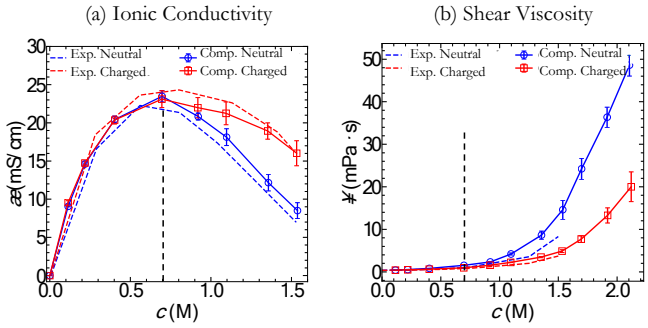

Figure 2. Ionic conductivity and dynamic viscosity as a function of solute molarity in two states of charge. Comparison of the MD models (solid lines and symbols with error bars) with experimental estimates (dashed lines with filling error margins).[63,64] *(a) Ionic conductivity vs concentration, with a maximum at 0.7 M. Above 1 M, the charged solution has higher conductivity compared to the neutral solutions. (b) Viscosity vs concentration. The onset of nonlinear increase of solution viscosity is indicated with the dashed vertical line.*

The critical concentration for ionic association

In this section, we show how a good estimate for the c_{crit} can be obtained from viscosity measurements. Concentration-dependent viscosity can be approximated by the Huggins equation[65] within the semi-dilute range of concentration,

$$\boldsymbol{\eta(c) = \eta_s\left(1 + [\eta]c + k_H([\eta]c)^2 + o(c^3)\right)} \quad (6)$$

where $\boldsymbol{\eta(c)}$ and $\boldsymbol{\eta_s}$ are the viscosities of solution and solvent respectively, $[\boldsymbol{\eta}]$ is the intrinsic solvent viscosity, which is a measure of solvent contribution to viscosity, and $\boldsymbol{k_H}$ is the Huggins coefficient that quantifies the interactions between solutes and solvent. For better fit, the equation is rearranged as

$$\boldsymbol{\eta_{red} = \frac{\eta/\eta_s - 1}{c} = [\eta] + k_H[\eta]^2 c} \quad (7)$$

where $\boldsymbol{\eta_{red}}$ is the reduced viscosity.

Fitting the parameters $[\boldsymbol{\eta}]$ and $\boldsymbol{k_H}$ to low-concentration data provides two key insights. First, inference of solute size and interactions. Size comes from $[\boldsymbol{\eta}]$, being larger for larger hydrodynamic diameter solutes. The nature of interactions comes from $\boldsymbol{k_H}$, where hydrodynamic interaction forms a baseline value, and larger values indicate additional interactions. Second, Eq.(7) allows for conductivity prediction by coupling solution viscosity to conductivity, e.g. via the Nernst-Einstein relation. In particular, one can predict the local maximum of conductivity at a critical concentration as a function of $[\boldsymbol{\eta}]$ and $\boldsymbol{k_H}$.

SI Figure 2 shows that Eq. (7) is a credible model when fit to the low-concentration data for neutral and charged systems, from measurement in SI Figure 2(a) and simulation in SI Figure 2(b). In the semi-dilute regime, the Huggins equation for reduced viscosity is linearly dependent on concentration, as in Eqn. (7). In SI Figure 2, it is clearly shown that the dependence deviates from linear at high concentrations, meaning the Huggins equation is no longer applicable. To find the most credible fit, we change the number of data points used for fit by changing the maximum concentration, as suggested in previous work,[64] and compare the Bayesian Information Criterion (BIC) of each fit. BIC is a criterion for model selection, and lower BIC is preferred. We find that for both systems, the minimum BICs, which suggest the most credible fits, are found when the maximum concentrations are 0.75 M, while those for simulated viscosities are found at 0.92 M and 0.70 M, respectively. The most credible fits are shown as solid lines in SI Figure 2, and the fit parameters are shown in Tab. 1.

Table 1. The most credible fit results of concentration-dependent reduced viscosities to the rearranged Huggins equation for neutral and charged solutions.

	c_{max} (M)	$[\eta]$ [L/mol]	k_H [-]	BIC [-]
Exp., neutral	0.75	0.42	16.92	0.61
Exp., charged	0.75	0.19	55.16	-10.97
Sim., neutral	0.92	0.50	20.45	-9.0
Sim., charged	0.70	0.44	12.06	-13.47

The Huggins coefficient, $\boldsymbol{k_H}$, represents the strength of interactions; the higher the $\boldsymbol{k_H}$, the larger the interactions between solutes and solvent molecules. For hard spheres with only steric effects and hydrodynamic interactions, $\boldsymbol{k_H}$= 0.992.[66] The Huggins coefficients determined here are much larger, suggesting that there are other interactions that contribute to the viscous dissipation, and the interactions between solutes and solvent molecules in both systems are one order of magnitude larger than the hydrodynamic

interaction. From the Nernst-Einstein[67] equation and the Stokes-Einstein[68] equation, the relation between ionic conductivity and dynamic viscosity can be written as

$$\sigma = \frac{ne^2}{6\pi r\eta} \quad (8)$$

where e is the elementary electric charge, r is the hydrodynamic radius of the ion, and n is the number of ions in the solution. Assuming that there is no ion association and the ion radius, , is a constant to all concentrations, we have,

$$\sigma \propto \frac{n}{\eta} \propto \frac{c}{1 + [\eta]c + k_H([\eta]c)^2} \quad (9)$$

The above function finds its maximum at $c_{crit} = \sqrt{\frac{1}{k_H[\eta]^2}}$. Using the fit results from Tab. 1, the critical concentrations where the ionic conductivity is maximized are 0.57 M and 0.73 M for neutral and charged systems respectively, while from simulation, the critical concentrations are 0.44 M and 0.66 M, respectively. These estimates are comfortably close despite the simplifications used in these derivations.

Since viscous dissipation occurs through structural relaxation, next, we present SAXS data, which is a direct probe for the (*t = 0*) ensemble-averaged structural order, which relaxes with time (*t > 0*), resulting in viscous dissipation.

Ionic association and network formation in SAXS

To verify that our charge renormalization approach correctly describes the ionic association in the systems, we used a more direct way to probe the networks of the associated ions using SAXS. A correlation peak in the scattering curve *I*(*Q*) arising from such networks implies the existence of a structural order at a length scale of 2π/*Q*, where *Q* is the momentum transfer vector corresponding to the peak maximum. Fortuitously, the $TFSI^-$ anions have high-Z atoms that strongly scatter 18 keV X-rays, thereby providing the contrast required for visualization of the ion association.

Figures 3a-f show the experimental and computed SAXS profiles for the systems studied; the experimental traces were taken from ref. [63] We compare the simulated SAXS for the two systems at different concentrations with the experimentally obtained traces in Figures 3b and 3e. The qualitative and quantitative agreement between the experimental (Figures 3b and 3e) and computational data (Figures 3a and 3d, respectively) validates our MD model to be representative of the real systems. It is seen that in the neutral solution, a medium-range order emerges at $c > c_{crit}$ as indicated by a strong correlation peak at lower *Q* than the solvent domain peak. By contrast, for the charged system, only a weak correlation peak or no peak is observed. Importantly, the order emerges in the same concentration range in which viscosity begins to increase rapidly with the concentration as shown in Figure 2b. See ref. [56] for more discussion of the network structure for the associated ions.

In Figures 3c and 3f we decompose SAXS into the linearized contributions for each constituent. It can be seen from Figure 3c that ordering of $TFSI^-$ anions is largely responsible for the features observed. Clearly the ionic association is stronger in the neutral system, manifesting itself through lower ionic conductivity, higher viscosity, and ion ordering into an expansive network.

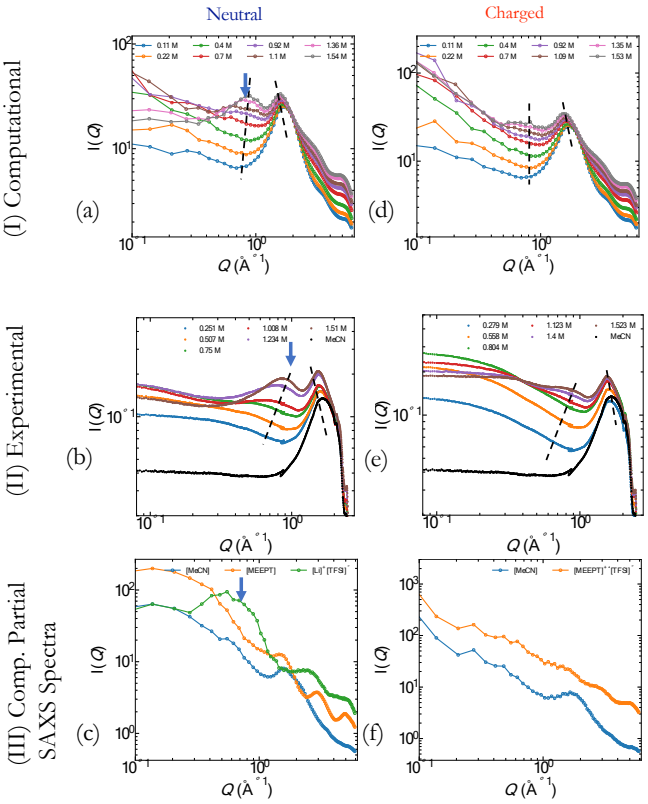

Figure 3. SAXS data illustrating the emergence of medium-range order in neutral and charged solutions of MEEPT. (a) MEEPT: LiTFSI in MeCN simulated SAXS. (b) MEEPT: Li^+TFSI^- in MeCN experimental SAXS. (c) Computational partial SAXS in a neutral solution, LiTFSI aggregation causes the emergence of a correlation peak above 1 M for MEEPT:LiTFSI in MeCN. (d) $MEEPT^{+*}TFSI^-$ in MeCN simulated SAXS. (e) $MEEPT^{+*}TFSI^-$ in MeCN experimental SAXS. (f) Computational partial SAXS in a charged solution..

Pair distribution functions (PDF) and the potential of mean force (PMF)

To recognize molecular forces responsible for this changeover, we examined interactions that satisfy the following two conditions: (1) they exhibit maximum variability when one compares the solutions below and above c_{crit} in each system, and (2) they exhibit maximum variability between the neutral and charged solutions of the same number of redoxmers (see the Introduction). As discussed earlier, SI Figure 3 shows the interaction dominating the manifested similarity of ionic conductivity below c_{crit}. Pair distribution functions for ionic and molecular species are shown in Figures 4a to 4f. We remind that PDF is the isotropic probability of finding a pair of molecules separated by a distance *r* as measured between their centers of mass. Figure 4a and 4d show PDF for the redoxmer self-pairing and ion pairing, respectively, which are the only interactions satisfying the two above mentioned criteria. From Figure 4a, for the redoxmer pairs, this probability of finding the two molecules 5.5 Å apart decreases as the concentration increases. As for the ion pairs in Figure 4d, in the neutral system, close Li^+TFSI^- pairs become more prevalent at higher concentrations, which assists the formation of the ion networks seen in our SAXS data.

Figures 4b to 4f show the corresponding potentials of mean force. The well depth of the profile gives the strength of interaction between the solutes, while the position of the minimum gives the interaction scale. From Figures 4b and 4c, which illustrate the PMF for redoxmer pairs in two states of charge, the effective size of the redoxmer molecule increases with increasing solute concentration and the molecule becomes less attractive. Figures 4e and 4f illustrate the PMF for the ion pairs. It can be seen from Figure 4e that the net effect of the concentration increase for the $MEEPT^{+\bullet}TFSI^-$ pairs is less attraction, hence less counter-ion screening. For the Li^+TFSI^- pairs, the well depth increases, and the ions become closer to each other due to reduced screening of the charges. This illustrates the difference between a small inorganic and a large organic cation. Figures 5a and 5b show the coordination of Li^+ cation as a function of redoxmer molarity. The number of associated MeCN molecules decreases from 4-5 in the dilute solution to < 2 in the concentrated one, as the solvent molecules become replaced by $TFSI^-$ anions and MEEPT chains. This solvent scarcity is the origin of the increased Li^+TFSI^- association seen in our SAXS data. For a larger $MEEPT^{+\bullet}$ cation, the association is weaker, so all effects due to ionic association are also weaker.

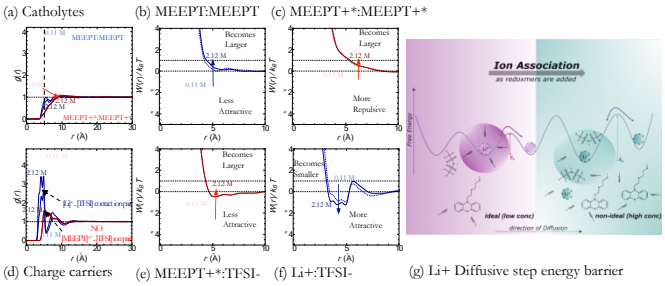

Figure 4. Solute-solute pair distribution function (PDF) g(r) and solution-averaged potential of mean force (PMF). Curves transparency ranges from light transparent at 0.11 M to dark zero-transparency at 2.12 M. Intermediate transparencies correspond to (0.22 M, 0.4 M, 0.7 M, 0.92 M, 1.1 M, 1.36 M, 1.54 M, 1.7 M, 1.92 M) in decreasing transparency level respectively. (a) MEEPT-MEEPT PDF in neutral and charged solutions. (b) MEEPT-MEEPT PMF in neutral solutions. (c) The same in the charged solutions. (d) Ion pair PDF in neutral and charged solutions. (e) MEEPT-TFSI PMF in charged solution. (f) Li-TFSI PMF in neutral solutions. (g) A schematic illustration of the energy barrier associated with electrolyte diffusion.

Ion diffusivity

As conceptualized in Figure 4g, tight ion association would exert strong drag on the associated ions, so their diffusion coefficients increasingly converge to similar values regardless of their size and shape (Figures 5c and 5d). For lithium cations, this is not the case as the small ion can hop between the ether chains of MEEPT molecules, but for the bulky $MEEPT^{+\bullet}$ cations one can expect the full convergence. Contrary to this expectation, Figure 5d shows 20% difference in the diffusion coefficients for $MEEPT^{+\bullet}$ and $TFSI^-$ even at high concentration, suggesting that the ion association remains relatively weak in this system over the entire concentration range that is limited by solubility of the corresponding salt. This is yet another indication of the difference in the strength of ionic association in the neutral and charged systems.

An additional difference between the neutral and charged solutions is the nature of effective forces between the solutes, whether it is attractive or repulsive in nature. In the van der Waals (VDW) picture,[69] the attractive force slowly varies as a function of separation, and hence can be treated as a simple mean field background potential holding the system together at a defined pressure and density. However, in the Li^+ containing system (see Figure 4f), the attractive first valley strongly varies as a function of distance. It plays an important role in determining the overall solution structure and dynamics and cannot be simply correlated to a corresponding VDW picture, exemplifying the collective modes of interaction. Network, gel-forming, and eventually percolated structures can be formed in the Li^+ containing system due to

its stronger attractive interactions with the anion in the absence of freely coordinating solvent. In addition, it has been shown that although similar structures can be obtained for a Lennard-Jones (LJ)-system through mapping to a corresponding VDW-picture, namely Weeks-Chandler-Andersen system, the viscous slowing down of the two systems is found to be quantitatively and qualitatively different over a broad density range, whereas the static pair correlations remain close.[70] This indicates the important role of attractive forces in determining different dynamical relaxations even for similar structurally correlated liquids. Here, from comparing the attractive tail of the PMF in Figures 4e and 4f, we can see the difference in the strength and range of attractive forces between the ions in neutral and charged solutions. Li^+TFSI^- attractive force is stronger and shorter-range, than the attraction force between $MEEPT^{+\cdot}TFSI^-$. The strong attractive forces between Li^+TFSI^- give rise to activated dynamics that are much slower[71] than the dynamical relaxations in the charged solution.[72–74]

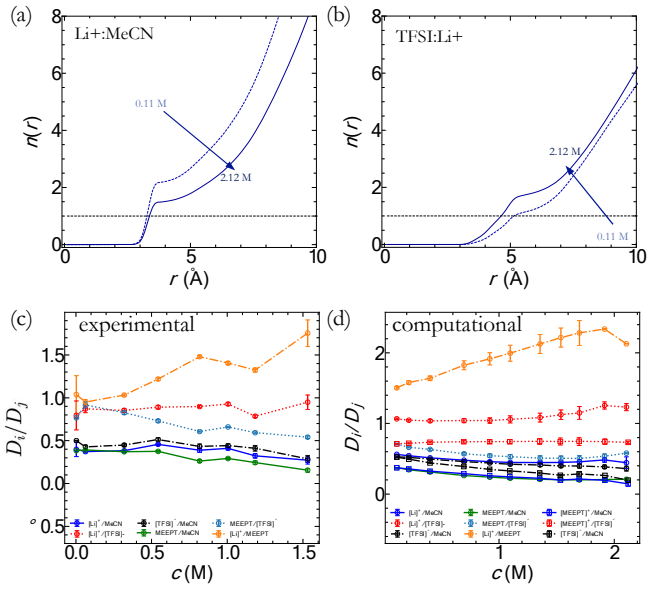

Figure 5. *(a) Coordination analysis of Li^+ cation as a function of solute molarity. Curves transparency ranges from light transparent at 0.11 M to dark zero-transparency at 2.12 M. Intermediate transparencies correspond to (0.22 M, 0.4 M, 0.7 M, 0.92 M, 1.1 M, 1.36 M, 1.54 M, 1.7 M, 1.92 M) in decreasing transparency level respectively. (b) $TFSI^-$ anion coordination with respect to Li^+ cation. Curve's transparencies mean the same as in panel a. (c) Experimental diffusivity ratios for different species in neutral solutions. (d) Computational diffusivity ratios for neutral and charged solutions.*

Ionic pairing and molecular clustering

One of the advantages of having a reliable MD model is the ability to compute quantities that are not directly accessible experimentally. Below, we turn to several such metrics characterizing molecular and ionic interactions in the two systems.

Figures 6a and 6b show the lifetime analysis of solute pairs in the neutral and charged solutions. Figure 6a shows the residence time correlation function for ion pairs, and Figure 6b shows the same quantity for MEEPT pairs. The correlation function is normalized to the initial number of pairs within the first coordination shell. As time evolves from this initial condition, an initially counted pair gets excluded from the count if the pair-distance becomes larger than the first minimum of the corresponding PDF. The residence time, area under the curve, of the ion and MEEPT pairs increases as the concentration ***c*** increases, signaling slower dynamics in viscous solutions. In a jump diffusion model, the molecules spend longer time close to each other before making a jump. As the concentration increases, the spatial domain visited by each molecule becomes smaller and these domains become increasingly isolated. This gradual localization can be seen in Figure 7, which depicts the projected trajectory of a randomly chosen solute molecule over 2 ns.

Another useful metric characterizes non-isotropic interactions between the redoxmer molecules. This metric complements PDF that makes no distinction between the stackable aromatic heads and the floppy ether tails. Figure 6c shows the mole fraction of pi-stacking for MEEPT molecules due to attraction between their benzene rings. Here the pi-stack has been defined by the interplane distance < 5.5 Å and the interplane angle < 25° as shown in Figure 6d. While in the isotropic PDF shown in Figures 4a and 4b the peak at 5.5 Å decreases as *c* increases, the fraction and lifetime of pi-stacks increases with the molarity, and such stacks contribute to slowing of the dynamics.

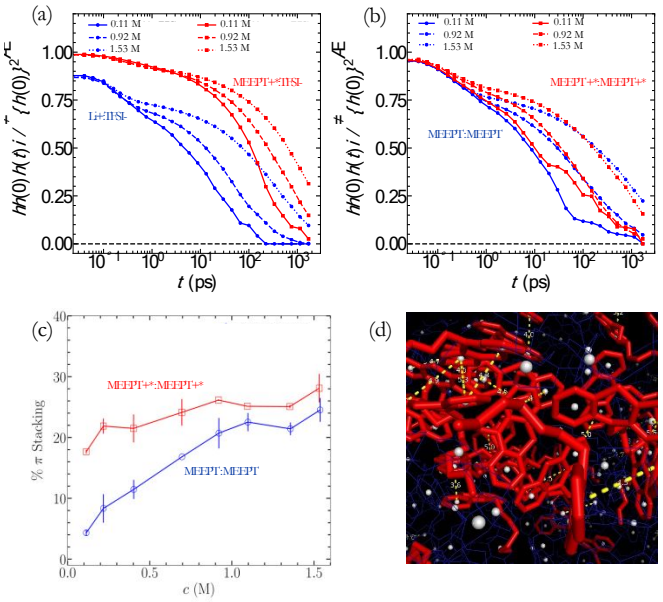

Figure 6. Residence lifetime analysis of solutes aggregates. (a) lifetime of ion pairs in neutral and charged solution. (b) lifetime for MEEPT self-pairing in both solutions. (c) MEEPT pi-stacking fraction as function of MEEPT molarity in different states of charge. (d) Graphical illustration of the pi-stacks in our MD simulations.

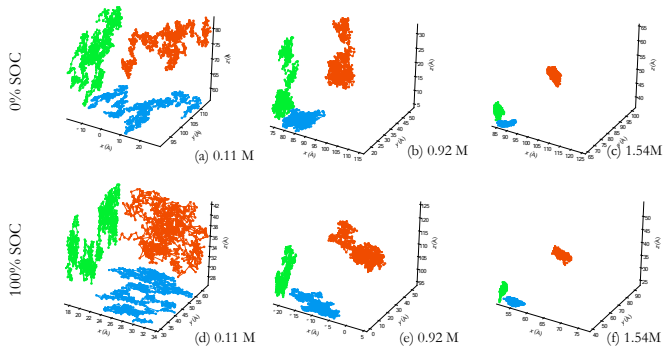

Figure 7. A 2 ns trajectory plot of a representative catholyte molecule at different redoxmer concentrations and state of charge. Different colors represent different projections for the trajectory.

Autocorrelation functions, viscoelasticity, and structural rigidity

Figures 8a-b contrast the neutral and charged systems by their ionic current and stress autocorrelation functions. In the neutral solution, the ionic current relaxation shows a negative correlation region that is not observed in the charged solution. We suggest that the tight 3-ion clusters in these strongly ionically associated solutions can lead to ionic current negative-correlation, since the ion pairs migrate in a correlated manner and in the same direction. Moreover, blocking and caging effects caused by the neutral MEEPT molecules to the lighter fast-moving Li^+ cations in the neutral solution can have a contribution to the negative current correlations. As for the stress relaxation, the autocorrelation functions rapidly approach zero, suggesting that the relaxation ends on the time scale of molecular motions. That means that the infinite frequency shear modulus G_∞ captures most of this behavior, especially in the highly crowded concentrated regime, validating our use of this modulus to characterize the onset of gelling in the solutions.

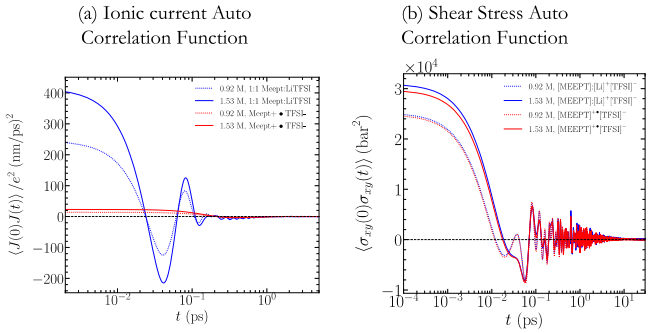

Figure 8. Solution ionic current and shear stress relaxation functions as a function of time for two solute concentrations above 0.7 M, which is the onset of variable dynamics noted in the respective transport coefficients in Figure 2. (a) Ionic current relaxation function versus time. The neutral solution exhibits a negative correlation region and hence oscillatory short-time relaxation as opposed to a monotonic relaxation in the charged solution. (b) Stress relaxation function versus time. Similarity in the stress relaxation behavior can be identified for the neutral and charged solutions at different time scales, in contrast to an observable variability in the initial elastic stress values.

Extending this insight, Figures 9a and 9b show a viscoelastic analysis of the neutral and charged systems. In Figure 9a, the G_∞ determines the stiffness of the solution, quantifying its ability to withstand deformation. Higher values of this modulus imply greater rigidity. We will use this parameter to rationalize the rapid increase in viscosity seen in Figure 2b; this increase corresponds to the system entering the gelling regime. In ref. [56], we reported the equally rapid decrease in solute and solvent diffusion coefficients and ionic conductivity seen in the same regime, so gelling impacts all dynamic properties of the systems. It is tempting to ascribe these behaviors to the increasing rigidity of networks of associated ions in the concentrated solutions that we observed in SAXS. Assuming the solution behaves as a single Maxwell element, in Figure 9b we computed the Maxwell relaxation time and plotted it as a function of *c*. It is seen that in the gelling regime this relaxation time increases considerably, indicating the stiffness of ion networks, especially in the neutral solution, where the ion association is particularly strong.

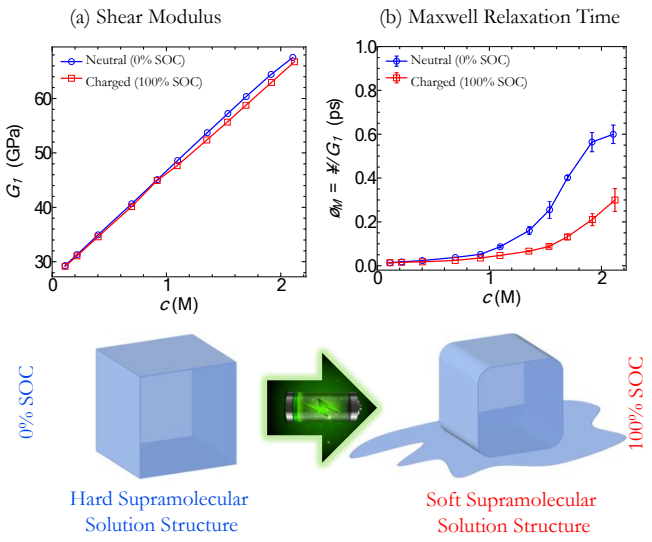

Figure 9. Viscoelasticity Analysis. (a) Infinite frequency dynamic modulus as a function of solute molarity in different states of charge. In neutral solutions (0% SOC), the rigidity is higher due to the smaller volume of Li^+TFSI^- aggregation, whereas in charged solutions (100% SOC), the solution dynamic dynamics is dominated by the increasingly repulsive coulomb force associated with increasing effective solute size. (b) Assuming the solution behaves as a single Maxwell element, a Maxwell relaxation time estimate is obtained, higher initial stress results in slower dynamics.

Our experimental and computational results point to a strong correlation between this rapid increase in stiffness of the neutral solutions and the equally rapid decrease in fluidity, conductivity, and diffusivity observed in this regime, which are all properties reflective of the collective modes of interaction and the emergent medium range order in this system seen in our SAXS data and MD simulations. In the systems where the ionic association is less strong which included the charged solution containing $MEEPT^{+\bullet}$ cations, the transition to this regime occurs at a higher concentration. Thus, we argue that as the electrochemical cell becomes charged, the concentrated electrolyte gradually transitions from a hard-matter-like medium with strong short-range attractive forces, to a soft-matter-like medium with weak and long-range forces. This transition is what causes the considerable increase in fluidity and diffusivity after charging the electrolyte in our idealized cell. As our argument is general, it suggests that in all systems with the cation exchange membranes a concentrated electrolyte (i) has *greater* structural rigidity and hence higher viscosity and lower conductivity in the discharged state, and (ii) this state approaches the critical regime at a *lower* concentration than the charged solution. The same applies to anion exchange membranes and anolyte (negative charge carrier) redoxmer molecules.

Conclusions

In this study, we have examined a non-aqueous electrolyte containing phenothiazine molecules which serve as a catholyte in redox flow cells. Discharged and simulated charged solutions were examined structurally and dynamically, and modeled using classical molecular dynamics. In both states of charge, the ionic conductivity passes through a maximum and then decreases as the ions associate, while the viscosity increases nonlinearly. This increase accelerates as the electrolyte enters the gelling regime, in which the collective modes of ionic interaction become predominant. We consider viscoelasticity to be most indicative of the transition into this regime, and we argue that the rapid increase in the Maxwell relaxation time is its most definitive signature. As the structure becomes rigid, the dynamic properties unravel, with the rapid decrease in fluidity and the precipitous loss of conductivity and diffusivity. This transition occurs at a *lower* concentration in the fully discharged systems compared to the fully charged ones, due to additional interactions that involve electrolyte ions that migrate between the compartments of the electrochemical cell. These interactions can be particularly strong for small cations, such as Li^+. Mastery of the collective modes for ionic association that define solution properties in crowded electrolytes is required for these electrolytes to become practically useful.

Author Contributions

Y Z initiated and directed the research. Hossam M. Farag conducted the molecular dynamics simulations, did the statistical analyses, and prepared the original draft. Aman Preet Kaur and Susan A. Odom synthesized the molecules for experimental measurements. Erik Sarnello, Xinyi Liu, and Tao Li conducted SAXS measurements. Ilya A. Shkrob conducted the conductivity and diffusion measurements. Yilin Wang and Randy Ewoldt conducted the viscosity measurements. All authors engaged in useful discussions throughout the research and preparation of the manuscript.

Conflicts of interest

"There are no conflicts to declare".

Acknowledgements

The research was financially supported by the Joint Center for Energy Storage Research (JCESR), an Energy Innovation Hub funded by the U.S. Department of Energy, Office of Science, Basic Energy Sciences. The submitted manuscript has been created by UChicago Argonne, LLC, Operator of Argonne National Laboratory ("Argonne").

Argonne, a U.S. Department of Energy Office of Science laboratory, is operated under Contract No. DE-AC02-06CH11357. The U.S. Government retains for itself, and others acting on its behalf, a paid-up nonexclusive, irrevocable worldwide license in the said article to reproduce, prepare derivative works, distribute copies to the public, and perform publicly and display publicly, by or on behalf of the Government. This manuscript is dedicated in memoriam of Professor Susan S. Odom, whose unending curiosity for fundamental scientific discovery and tackling challenges continues to inspire us all.

References

1 J. Self, K. D. Fong and K. A. Persson, Transport in Superconcentrated LiPF 6 and LiBF 4 /Propylene Carbonate Electrolytes, *ACS Energy Lett*, 2019, **4**, 2843–2849.

2 R. M. Fuoss, Properties of Electrolytic Solutions., *Chem Rev*, 1935, **17**, 27–42.

3 R. M. Fuoss, Review of the theory of electrolytic conductance, *J Solution Chem*, 1978, **7**, 771–782.

4 L. Onsager, The Motion of Ions: Principles and Concepts, *Science (1979)*, 1969, **166**, 1359–1364.

5 L. Onsager and R. M. Fuoss, Irreversible Processes in Electrolytes. Diffusion, Conductance and Viscous Flow in Arbitrary Mixtures of Strong Electrolytes, *J Phys Chem*, 1932, **36**, 2689–2778.

6 L. Onsager, Theories of Concentrated Electrolytes., *Chem Rev*, 1933, **13**, 73–89.

7 Jean Pierre Boon and S. Yip, *Molecular Hydrodynamics*, McGraw-Hill International Book, Mineola, NY, First., 1980.

8 L. Onsager and S. W. Provencher, Relaxation effects in associating electrolytes, *J Am Chem Soc*, 1968, **90**, 3134–3140.

9 L. Onsager and S. K. Kim, The Relaxation Effects in Mixed Strong Electrolytes, *J Phys Chem*, 1957, **61**, 215–229.

10 C. A. Kraus, The present status of the theory of electrolytes, *Bulletin of the American Mathematical Society*, 1938, **44**, 361–384.

11 K. Xu, Nonaqueous Liquid Electrolytes for Lithium-Based Rechargeable Batteries, *Chem Rev*, 2004, **104**, 4303–4418.

12 Y. Marcus and G. Hefter, Ion Pairing, *Chem Rev*, 2006, **106**, 4585–4621.

13 H. B. G. Casimir, On Onsager's Principle of Microscopic Reversibility, *Rev Mod Phys*, 1945, **17**, 343–350.

14 H. Falkenhagen, The Principal Ideas in the Interionic Attraction Theory of Strong Electrolytes, *Rev Mod Phys*, 1931, **3**, 412–426.

15 Y. Yamada and A. Yamada, Review—Superconcentrated Electrolytes for Lithium Batteries, *J Electrochem Soc*, 2015, **162**, A2406–A2423.

16 T. M. Chang and L. X. Dang, Li+ solvation and kinetics of Li+-BF4-/PF6- ion pairs in ethylene carbonate. A molecular dynamics study with classical rate theories, *Journal of Chemical Physics*, , DOI:10.1063/1.4991565.

17 G. Markovich, L. Perera, M. L. Berkowitz and O. Cheshnovsky, The solvation of Cl-, Br-, and I- in acetonitrile clusters: Photoelectron spectroscopy and molecular dynamics simulations, *Journal of Chemical Physics*, 1996, **105**, 2675–2685.

18 R. Semino, G. Zaldívar, E. J. Calvo and D. Laria, Lithium solvation in dimethyl sulfoxide-acetonitrile mixtures, *Journal of Chemical Physics*, , DOI:10.1063/1.4902837.

19 X. Chen and D. G. Kuroda, Molecular motions of acetonitrile molecules in the solvation shell of

lithium ions, *Journal of Chemical Physics*, , DOI:10.1063/5.0024486.

20 L. X. Dang and T. M. Chang, Rate theory of solvent exchange and kinetics of Li+ - BF4-/PF6- ion pairs in acetonitrile, *Journal of Chemical Physics*, , DOI:10.1063/1.4961904.

21 K. L. Gering, Prediction of Electrolyte Conductivity: Results from a Generalized Molecular Model Based on Ion Solvation and a Chemical Physics Framework, *Electrochim Acta*, 2017, **225**, 175–189.

22 K. L. Gering, Prediction of electrolyte viscosity for aqueous and non-aqueous systems: Results from a molecular model based on ion solvation and a chemical physics framework, *Electrochim Acta*, 2006, **51**, 3125–3138.

23 D. M. Seo, O. Borodin, S.-D. Han, P. D. Boyle and W. A. Henderson, Electrolyte Solvation and Ionic Association II. Acetonitrile-Lithium Salt Mixtures: Highly Dissociated Salts, *J Electrochem Soc*, 2012, **159**, A1489–A1500.

24 D. M. Seo, O. Borodin, D. Balogh, M. O'Connell, Q. Ly, S.-D. Han, S. Passerini and W. A. Henderson, Electrolyte Solvation and Ionic Association III. Acetonitrile-Lithium Salt Mixtures–Transport Properties, *J Electrochem Soc*, 2013, **160**, A1061–A1070.

25 S.-D. Han, O. Borodin, J. L. Allen, D. M. Seo, D. W. McOwen, S.-H. Yun and W. A. Henderson, Electrolyte Solvation and Ionic Association IV Acetonitrile-Lithium Difluoro(oxalato)borate (LiDFOB) Mixtures, *J Electrochem Soc*, 2013, **160**, A2100–A2110.

26 S.-D. Han, O. Borodin, J. L. Allen, D. M. Seo, D. W. McOwen, S.-H. Yun and W. A. Henderson, Electrolyte Solvation and Ionic Association, *J Electrochem Soc*, 2013, **160**, A2100–A2110.

27 D. Bedrov, J.-P. Piquemal, O. Borodin, A. D. MacKerell, B. Roux and C. Schröder, Molecular Dynamics Simulations of Ionic Liquids and Electrolytes Using Polarizable Force Fields, *Chem Rev*, 2019, **119**, 7940–7995.

28 I. A. Shkrob, T. Li, E. Sarnello, L. A. Robertson, Y. Zhao, H. Farag, Z. Yu, J. Zhang, S. R. Bheemireddy, Y. Z, R. S. Assary, R. H. Ewoldt, L. Cheng and L. Zhang, Self-Assembled Solute Networks in Crowded Electrolyte Solutions and Nanoconfinement of Charged Redoxmer Molecules, *J Phys Chem B*, 2020, **124**, 10226–10236.

29 J. Zhang, R. E. Corman, J. K. Schuh, R. H. Ewoldt, I. A. Shkrob and L. Zhang, Solution Properties and Practical Limits of Concentrated Electrolytes for Nonaqueous Redox Flow Batteries, *Journal of Physical Chemistry C*, 2018, **122**, 8159–8172.

30 Y. Zhao, Z. Yu, L. A. Robertson, J. Zhang, Z. Shi, S. R. Bheemireddy, I. A. Shkrob, Y Z, T. Li, Z. Zhang, L. Cheng and L. Zhang, Unexpected electrochemical behavior of an anolyte redoxmer in flow battery electrolytes: solvating cations help to fight against the thermodynamic–kinetic dilemma, *J Mater Chem A Mater*, 2020, **8**, 13470–13479.

31 L. A. Robertson, Z. Li, Y. Cao, I. A. Shkrob, M. Tyagi, K. C. Smith, L. Zhang, J. S. Moore and Y. Z, Observation of Microheterogeneity in Highly Concentrated Nonaqueous Electrolyte Solutions, *J Am Chem Soc*, 2019, **141**, 8041–8046.

32 M. Li, C. Wang, Z. Chen, K. Xu and J. Lu, New Concepts in Electrolytes, *Chem Rev*, 2020, **120**, 6783–6819.

33 G. L. Soloveichik, Flow Batteries: Current Status and Trends, *Chem Rev*, 2015, **115**, 11533–11558.

34 M. Winter and R. J. Brodd, What Are Batteries, Fuel Cells, and Supercapacitors?, *Chem Rev*, 2004, **104**, 4245–4270.

35 Y. Wang, A. Preet, T. M. Suduwella, Z. Yu, L. Cheng and S. A. Odom, Viscous flow properties and hydrodynamic diameter of phenothiazine-based redox-active molecules in different supporting salt environments, 1–21.

36 M. Valiev, E. J. Bylaska, N. Govind, K. Kowalski, T. P. Straatsma, H. J. J. Van Dam, D. Wang, J. Nieplocha, E. Apra, T. L. Windus and W. A. de Jong, NWChem: A comprehensive and scalable open-source solution for large scale molecular simulations, *Comput Phys Commun*, 2010, **181**, 1477–1489.

37 A. D. Becke, Density-functional thermochemistry. III. The role of exact exchange, *J Chem Phys*, 1993, **98**, 5648–5652.

38 C. Lee, W. Yang and R. G. Parr, Development of the Colle-Salvetti correlation-energy formula into a functional of the electron density, *Phys Rev B*, 1988, **37**, 785–789.

39 A. V Marenich, C. J. Cramer and D. G. Truhlar, Universal Solvation Model Based on Solute Electron Density and on a Continuum Model of the Solvent Defined by the Bulk Dielectric Constant and Atomic Surface Tensions, *J Phys Chem B*, 2009, **113**, 6378–6396.

40 Z. Li, L. A. Robertson, I. A. Shkrob, K. C. Smith, L. Cheng, L. Zhang, J. S. Moore and Y. Z, Realistic Ion Dynamics through Charge Renormalization in Nonaqueous Electrolytes, *J Phys Chem B*, 2020, **124**, 3214–3220.

41 M. J. Abraham, T. Murtola, R. Schulz, S. Páll, J. C. Smith, B. Hess and E. Lindah, Gromacs: High performance molecular simulations through multi-level parallelism from laptops to supercomputers, *SoftwareX*, 2015, **1–2**, 19–25.

42 W. L. Jorgensen, D. S. Maxwell and J. Tirado-Rives, Development and Testing of the OPLS All-Atom Force Field on Conformational Energetics and Properties of Organic Liquids, *J Am Chem Soc*, 1996, **118**, 11225–11236.

43 A. Allouche, Software News and Updates Gabedit — A Graphical User Interface for Computational Chemistry Softwares, *J Comput Chem*, 2012, **32**, 174–182.

44 G. Bussi, D. Donadio and M. Parrinello, Canonical sampling through velocity rescaling, *J Chem Phys*, 2007, **126**, 014101.

45 M. Parrinello and A. Rahman, Polymorphic transitions in single crystals: A new molecular dynamics method, *J Appl Phys*, 1981, **52**, 7182–7190.

46 T. Darden, D. York and L. Pedersen, Particle mesh Ewald: An N ·log(N) method for Ewald sums in large systems, *J Chem Phys*, 1993, **98**, 10089–10092.

47 N. P. Walter, A. Jaiswal, Z. Cai and Y. Zhang, LiquidLib: A comprehensive toolbox for analyzing classical and ab initio molecular dynamics simulations of liquids and liquid-like matter with applications to neutron scattering experiments, *Comput Phys Commun*, 2018, **228**, 209–218.

48 A. P. Kaur, O. C. Harris, N. H. Attanayake, Z. Liang, S. R. Parkin, M. H. Tang and S. A. Odom, Quantifying Environmental Effects on the Solution and Solid-State Stability of a Phenothiazine Radical Cation, *Chemistry of Materials*, 2020, **32**, 3007–3017.

49 J. D. Milshtein, A. P. Kaur, M. D. Casselman, J. A. Kowalski, S. Modekrutti, P. L. Zhang, N. Harsha Attanayake, C. F. Elliott, S. R. Parkin, C. Risko, F. R. Brushett and S. A. Odom, High current density, long duration cycling of soluble organic active species for non-aqueous redox flow batteries, *Energy Environ Sci*, 2016, **9**, 3531–3543.

50 A. P. Kaur, N. E. Holubowitch, S. Ergun, C. F. Elliott and S. A. Odom, A Highly Soluble Organic Catholyte for Non-Aqueous Redox Flow Batteries, *Energy Technology*, 2015, **3**, 476–480.

51 M. D. Casselman, A. P. Kaur, K. A. Narayana, C. F. Elliott, C. Risko and S. A. Odom, The fate of phenothiazine-based redox shuttles in lithium-ion batteries, *Physical Chemistry Chemical Physics*, 2015, **17**, 6905–6912.

52 A. P. Kaur, C. F. Elliott, S. Ergun and S. A. Odom, Overcharge Performance of 3,7-Bis(trifluoromethyl)- *N* -ethylphenothiazine at High Concentration in Lithium-Ion Batteries, *J Electrochem Soc*, 2016, **163**, A1–A7.

53 K. A. Narayana, M. D. Casselman, C. F. Elliott, S. Ergun, S. R. Parkin, C. Risko and S. A. Odom, N-Substituted Phenothiazine Derivatives: How the Stability of the Neutral and Radical Cation Forms Affects Overcharge Performance in Lithium-Ion Batteries, *ChemPhysChem*, 2015, **16**, 1179–1189.

54 A. P. Kaur, S. Ergun, C. F. Elliott and S. A. Odom, 3,7-Bis(trifluoromethyl)-N-ethylphenothiazine: a redox shuttle with extensive overcharge protection in lithium-ion batteries, *J. Mater. Chem. A*, 2014, **2**, 18190–18193.

55 S. Ergun, C. F. Elliott, A. P. Kaur, S. R. Parkin and S. A. Odom, Overcharge performance of 3,7-disubstituted N-ethylphenothiazine derivatives in lithium-ion batteries, *Chem. Commun.*, 2014, **50**, 5339–5341.

56 I. A. Shkrob, L. A. Robertson, Z. Yu, R. S. Assary, L. Cheng, L. Zhang, E. Sarnello, X. Liu, T. Li, A. Preet Kaur, T. Malsha Suduwella, S. A. Odom, Y. Wang, R. H. Ewoldt, H. M. Farag and Y. Z, Crowded electrolytes containing redoxmers in different states of charge: Solution structure, properties, and fundamental limits on energy density, *J Mol Liq*, 2021, **334**, 116533.

57 Y. Zhao, J. Zhang, G. Agarwal, Z. Yu, R. E. Corman, Y. Wang, L. A. Robertson, Z. Shi, H. A. Doan, R. H. Ewoldt, I. A. Shkrob, R. S. Assary, L. Cheng, V. Srinivasan, S. J. Babinec and L. Zhang, TEMPO allegro: liquid catholyte redoxmers for nonaqueous redox flow batteries, *J Mater Chem A Mater*, 2021, **9**, 16769–16775.

58 M. Li, S. A. Odom, A. R. Pancoast, L. A. Robertson, T. P. Vaid, G. Agarwal, H. A. Doan, Y. Wang, T. M. Suduwella, S. R. Bheemireddy, R. H. Ewoldt, R. S. Assary, L. Zhang, M. S. Sigman and S. D. Minteer, Experimental Protocols for Studying Organic Non-aqueous Redox Flow Batteries, *ACS Energy Lett*, 2021, **6**, 3932–3943.

59 N. H. Attanayake, Z. Liang, Y. Wang, A. P. Kaur, S. R. Parkin, J. K. Mobley, R. H. Ewoldt, J. Landon and S. A. Odom, Dual function organic active materials for nonaqueous redox flow batteries, *Mater Adv*, 2021, **2**, 1390–1401.

60 Y. Wang, A. P. Kaur, N. H. Attanayake, Z. Yu, T. M. Suduwella, L. Cheng, S. A. Odom and R. H. Ewoldt, Viscous flow properties and hydrodynamic diameter of phenothiazine-based redox-active molecules in different supporting salt environments, *Physics of Fluids*, 2020, **32**, 083108.

61 X. Liu, Z. Yu, E. Sarnello, K. Qian, S. Seifert, R. E. Winans, L. Cheng and T. Li, Microscopic Understanding of the Ionic Networks of “Water-in-Salt” Electrolytes, *Energy Material Advances*, 2021, **2021**, 1–9.

62 X. Liu, S.-C. Lee, S. Seifer, R. E. Winans, L. Cheng, Y. Z and T. Li, Insight into the nanostructure of “water in salt” solutions: A SAXS/WAXS study on imide-based lithium salts aqueous solutions, *Energy Storage Mater*, 2022, **45**, 696–703.

63 I. A. Shkrob, L. A. Robertson, Z. Yu, R. S. Assary, L. Cheng, L. Zhang, E. Sarnello, X. Liu, T. Li, A. Preet Kaur, T. Malsha Suduwella, S. A. Odom, Y. Wang, R. H. Ewoldt, H. M. Farag and Y. Z, Crowded Electrolytes Containing Redoxmers in Different States of Charge: Solution Structure, Properties, and Fundamental Limits on Power Density, *J Mol Liq*, 2021, **334**, 116533.

64 Y. Wang, A. P. Kaur, N. H. Attanayake, Z. Yu, T. M. Suduwella, L. Cheng, S. A. Odom and R. H. Ewoldt, Viscous flow properties and hydrodynamic diameter of phenothiazine-based redox-active molecules in different supporting salt environments, *Physics of Fluids*, 2020, **32**, 083108.

65 M. L. Huggins, The Viscosity of Dilute Solutions of Long-Chain Molecules. IV. Dependence on Concentration, *J Am Chem Soc*, 1942, **64**, 2716–2718.

66 G. K. Batchelor, The effect of Brownian motion on the bulk stress in a suspension of spherical particles, *J Fluid Mech*, 1977, **83**, 97–117.

67 E. R. Bittner, Chemical Dynamics in the Condensed Phases: Relaxation, Transfer, and Reactions in Condensed Molecular Systems By Abraham Nitzan (Tel Aviv University). Oxford University Press: Oxford, New York. 2006. xxii + 720 pp. $89.50. ISBN 0-19-852979-1., *J Am Chem Soc*, 2006, **128**, 17156–17157.

68 A. Einstein, University of Zurich, 1905.

69 D. Chandler, J. D. Weeks and H. C. Andersen, Van der waals picture of liquids, solids, and phase transformations, *Science (1979)*, 1983, **220**, 787–794.

70 L. Berthier and G. Tarjus, Nonperturbative Effect of Attractive Forces in Viscous Liquids, *Phys Rev Lett*, 2009, **103**, 170601.

71 A. Ghosh and K. S. Schweizer, Microscopic theory of the influence of strong attractive forces on the activated dynamics of dense glass and gel forming fluids, *J Chem Phys*, 2019, **151**, 244502.

72 H. Tanaka, J. Meunier and D. Bonn, Nonergodic states of charged colloidal suspensions: Repulsive and attractive glasses and gels, *Phys Rev E*, 2004, **69**, 031404.

73 Y. M. Joshi, Dynamics of Colloidal Glasses and Gels, *Annu Rev Chem Biomol Eng*, 2014, **5**, 181–202.

74 Z. Zhou, D. Jia, J. V. Hollingsworth, H. Cheng and C. C. Han, From repulsive to attractive glass: A rheological investigation, *J Chem Phys*, 2015, **143**, 234901.